Design and test of a beam profile monitoring device for low intensity radioactive beams

P. N. Ostroumov, P. Billquist, M. Portillo,[a] and W. Q. Shen
Physics Division, Argonne National Laboratory, 9700 South Cass Avenue, Argonne, Illinois 60439

(Received 2 August 2001; accepted for publication 1 October 2001)

Development efforts have gone into the construction and performance testing of a device that can be used to provide snap shot images of the beam profile. It is intended to function even at very low ion intensities, such as those expected from a rare-isotope accelerator. Intensity profiles and emittance analysis are among the most critical tools used for optimizing beam transport through accelerators. This article describes the design and performance of a beam image monitor. The device is sensitive at a wide dynamic range which spans from $\sim 10^2$ to $\sim 10^{12}$ pps. With the advent of double-plane slits or a pepper pot plate, this system can be used to scan transverse emittance profiles in both the $x-x'$ and $y-y'$ phase space planes, simultaneously. Conventional diagnostic devices used for heavy ion accelerators generally require at least 10^9 pps intensity to carry out similar diagnostics, which is not practical when considering beams with very low intensities, such as rare isotope beams. Furthermore, the detection system used here can be used for a wide range of incident ion velocities. Compared with solid-state detectors and scintillators that are inserted directly into the beam, this type of detection system is less susceptible to beam induced damage resulting in longer lifetimes and less maintenance. The test was done using single charge state Kr beams at energies ranging from 3.6 to 18 keV/u. The device's sensitivity was monitored for intensities below 10^{12} pps and an emittance scan was recorded and analyzed. The spatial resolution was characterized by comparing the emittance profile with that obtained by a wire scanning device which had better resolution but was sensitive only to intensities above 10^{11} pps. Recently, the device has been used to aid in the transport of ~ 6 MeV/u radioactive beams, such as ^{17}F, produced by pickup reactions with a gas cell target at the ATLAS accelerator facility.
[DOI: 10.1063/1.1419227]

I. DESIGN FEATURES

A layout of the beam image monitor (BIM) is illustrated in Fig. 1. The beam comes in from the left and passes through any necessary slits or apertures, such as a pepper pot plate. Particles strike a flat aluminum surface that is oriented at 45° relative to the beam direction. The plate serves as a dynode since the ion signal is converted to a burst of secondary electrons (SEs). These secondaries are promptly accelerated by a 5–15 kV potential imposed by a grid lying parallel to and 5 mm from the surface. Motion feedthroughs are used to insert the aluminum foil dynode and a dual slit plate upstream. A diagram illustrating a Simion 7[1] simulation of this process is shown in Fig. 2. We note that the beam cross section in the horizontal plane will appear $\sqrt{2}$ times large due to the 45° tilt relative to the beam coordinate system of the beam which is shown in the diagram.

A position sensitive microchannel plate (MCP) is excited by the secondary electrons and further amplifies the signal induced by the secondaries. The MCP is parallel to the conversion surface as well and lies 47 mm after the grid. The accelerating potential is distributed evenly enough such that the electrons are accelerated perpendicular to the conversion surface, thus the system may be used to map the ion beam intensity along the transverse plane.

The actual detection of the signal is done with the combination of a phosphor screen and a light sensitive detector. A monochromatic charge coupled device (CCD) would be sufficient for detecting the light signal; however, we chose a charge integrating device (CID) since it has less cross sensor induced noise as well as less thermal induced noise.

A dual MCP detection system was actually used here to obtain a high gain. The second MCP lies 0.5 mm behind the first, such that the channel holes align. Both MCPs are identical at 41 mm in diameter and can sustain a maximum bias of 1000 V_{dc} each. A resistive circuit was constructed to allow both MCPs to have equal biases and runoff of a single power supply. The dual MCP system has a combined maximum gain of 4×10^7.

About 0.5 mm behind the second MCP there is a type P-20 phosphor plate. It is biased at 3 kV relative to the MCP output to convert the accelerated electron's energy into photons of predominantly 560 nm wavelength. The quantum efficiency is estimated to be about 0.063 photons/eV/electron in this wavelength region.[2]

The image is demagnified by a factor of 3 and transmitted to the CID sensor via a fiber optic transport system. The demagnifying element is a fused, tapered fiber optic bundle that goes from 41 to 13.7 mm in diameter. Between the end

[a]Author to whom correspondence should be addressed; electronic mail: portillo@phy.anl.gov

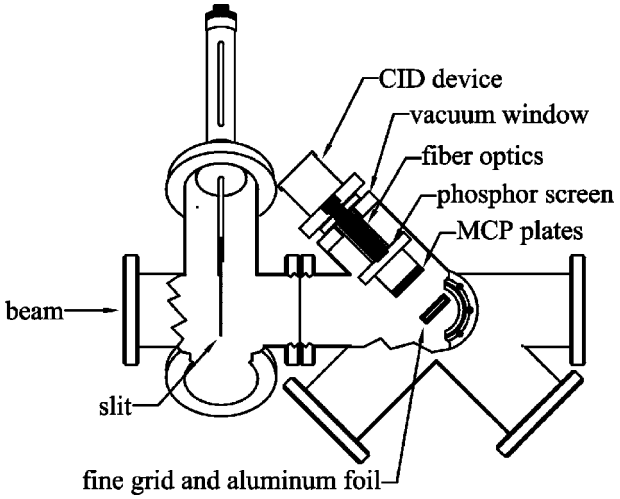

FIG. 1. Diagram of the BIM.

of the tapered rod and the phosphor screen is a 13.7 mm diam fiber optic rod in direct contact, such that loss of light in minimized. The fiber optic rods are both made of fused glass, optical fiber rods with polished faces. The combined optical system has about 15% total transmission efficiency for most of the visible spectrum of light. The spatial resolution for a single particle exciting the MCP surface directly is better than 0.15 mm according to the manufacturer's specifications[3] and the reported results of Shapira and others.[4]

The CID sensors accumulate a charge that is directly proportional to the total photon flux absorbed at each respective location. The charge is integrated over a 33 ms period and each sensor is discharged after each read. The thermal noise of the CID sensor array limits the integration period and the amplification gain; however, cooling the sensor and electronics to about $-10\,^{\circ}\mathrm{C}$ improves the performance over room temperature operation. We chose to test the performance of this system at room temperature in this study.

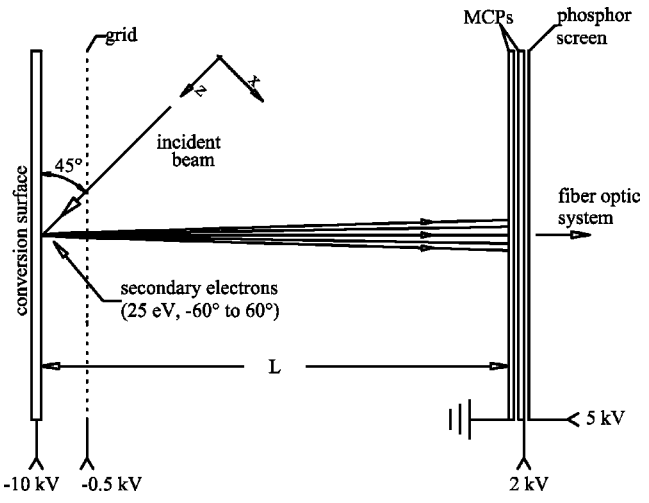

FIG. 2. Diagram secondary electron collection region of BIM. Trajectories of electrons exiting the surface at angles ranging from $-60°$ to $60°$ with a kinetic energy of 25 eV are simulated with Simon using a 330 μm spaced grid. Bias potential used for each element is shown along the bottom. The beam coordinate system is oriented such that the z axis points in the direction that the beam travels.

The electronics within the camera allow the CID sensors to be read out in the RS-170 standard of rastering images. The signal is amplified and then fed into a PCI-1408 frame grabber circuit board. The board features its own amplification with programmable gain to processes the signal before it is delivered to an 8-bit flash analog to digital converter. This ADC is capable of sampling at up to 16.5 MHz, but need only function at 12.3 MHz in the RS-170 raster mode. The images may be digitally processed in real time with the use of National Instruments IMAQ software and may be stored for later reference or processing. The image signal may also be split to be monitored simultaneously with a TV monitor. The beam imaging system including MCP, phosphor screen, fiber optic rod, and CID camera was purchased commercially from the Calutron Research Corporation.[3]

The PC also has a stepper motor control board and encoder reference input. This allows us to control and monitor the linear feedthrough devices that introduce the conversion surface and the upstream slit pattern. The conversion surface may be removed to allow the beam to pass when detection is no longer necessary. The position of the slit is monitored with a differential encoder.

A group at the Leuven facility has reported the performance of a similar device.[5] The most notable feature of their setup is the use of microsphere plates (MSPs) instead of a dual MCP as used here. Although its known to sustain higher pressure conditions than the MCP, the MSP generally exhibits artificial structure resulting in poor resolution. The Leuven device has a limited grid potential of 5 kV and little is referenced about the effects the grid spacing has on its performance. In the BIM device here we can apply up to a 15 kV potential without thermionic emission and breakdown at pressures better than 10^{-6} Torr. Furthermore, they use a CCD lens camera for detection from the phosphor screen while a CID sensor and fiber optics is utilized here instead. Other systems based on secondary electron emission have been tested or are underway for the measurement of ion beam transverse and longitudinal profiles.[6]

In another study conducted by Shapira and others, a detection system similar to the one constructed here was used with thin foils of carbon or aluminized Mylar instead of a polished aluminum surface.[4] They utilized a similar MCP detection system to study fast timing and position resolution with the use of a position-sensitive timing detector. Their results support some of the conclusions found in this study.

II. BEAM INTENSITY CALIBRATION

A test bench at the "8°+27° West" beam line at the Argonne Dynamitron accelerator was configured to test the performance of the detection system with stable $^{84}Kr^{+1}$ dc beams. The beam energy used ranged from 300 keV to 1.5 MeV for our experiments. Two dipoles bending in the same direction are used to select the isotope of interest over a 15 m long transport line and a quadrupole doublet refocuses the beam as is delivered to the target region.

The plasma source of the accelerator typically delivers beams at the tens of microamperes range in steady operation.

An independent channeltron detection system was set up directly upstream to monitor the intensity. This detector consists of an aluminum cup used as a dynode for collecting secondary electrons at the channeltron for ion detection. The cup floats at a very high impedance to allow measurement of tens of picoamps with a current integrator. This detector can be readily calibrated for each measurement by simultaneously applying two grid attenuators to suppress the beam intensities down to the 10^3 pps level for a $^{84}Kr^+$ beam at 12 keV/u. The detection efficiency of the channeltron detection system was measured to be $1.7\% \pm 0.1\%$.

The two attenuators are 1.5 m apart with a 27° bend dipole between and have known transmission values. Four-jaw slits are used for lowering down the intensity further as well as for finding the exact location of the beam position. Once calibrated, the channeltron detection system served as the reference to determine the beam current.

III. PROPERTIES OF SECONDARY ELECTRONS AND EFFECT ON DETECTOR

A significant amount of signal amplification is attributable to the collision of the ion with the aluminum dynode. The excitations from the colliding projectile at the dynode result in the ejection of other ions, neutrals, photons, and electrons. The energy and angle distributions of ejected SE have been studied by Rothard and others[7] and find that the angular distribution of the ejected electrons tends to obey a $\cos\theta$ distribution, yet with no dependence on the angle of incidence of the projectile. When surface roughness is appreciable the intensity seems to drop off more rapidly when sampling away from the surface normal.

The energy distribution of secondaries tends to exhibit a feature that is predominantly independent of the combination of projectile and target used. The distributions tend to exhibit a sharp peak at 2.1 ± 0.3 eV that contains ~85% of the total distribution. The rest of the distribution lies along a decaying exponential like curve with some structure present as a result of Auger and kinematic effects.[7]

The average number of secondary electrons ejected per ion event γ depends on many characteristics of the projectile/surface combination. A general argument can be applied for understanding why SE flux is attributable to the excitations close to the surface. The range even for 0.3 keV/u ^{84}Kr is about 200 Å and most of the energy is deposited evenly along the path of the collision cascade. The mean free path of electrons with energies even at 20–100 eV is 3–5 Å;[8] therefore, it is conceivable that only the energy deposited within the first few layers from the surface contributes to the SE flux. For these reasons the average number of ejected electrons turns out to be proportional to the electronic stopping power dE/dx of the projectile/target combination.[9] The energy deposited close to the surface also increases with the angle of incidence, and studies have shown that the secondaries give a distribution proportional to $\sec\theta$.[10]

The number of secondary electrons ejected per ion event can be characterized by a Polya, or negative binomial, distribution as shown by Dietz and Shefield.[9,10] Binary collisions between atoms are generally described best by a Poisson distribution; however, the effects of the bulk surface on the escaping electrons results in a broadening that depends much on the ion/target species as well as other surface properties. The result is an overall growth in the variance σ for the distribution. For example, it had been observed that a 30 keV Cs^+ beam impinging on an oxygen treated Cu–2%Be surface gives ~10% larger σ than expected form a Poisson distribution at the measured γ.[11] The broadening affects the efficiency of detection and makes it impractical to apply the technique for discriminating between different particles.

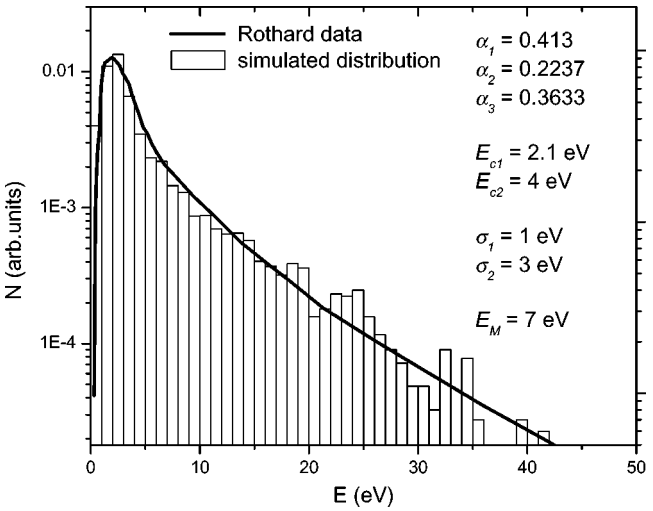

FIG. 3. Simulation of energy distribution (bar graph) compared to the experimental data of Rothard. The parameters used with the probability density function are listed.

In this study we measure the overall electron flux by applying a potential to the dynode to suppress the electrons and subtracting the ion current. At an incident angle of 45° we obtain ~12 e^-/ion for 1.5 MeV $^{84}Kr^{+1}$ on the untreated aluminum surface. Building up an oxide layer at the surface and using materials such as Cu–2%Be can increase γ; however, we use an untreated surface since it is less susceptible to surface degradation over long exposures to heavy ions.

Trajectory simulations were carried out using Simion 7 to determine the broadening effects caused by the overall drift and microlensing at the grid. Monte Carlo techniques were applied to simulate the energy and angular distribution of the secondaries. The distribution of angles is taken to be $\cos\theta$ in form. The combination of two Gaussians and a Maxwellian function was utilized to form a probability density that best fits the data of Rothard[7] for the energy distribution. The function is expressed by

$$p(x) = \frac{\alpha_1}{\sqrt{2\pi\sigma_1^2}} \exp[-(E-E_{C1})^2/2\sigma_1^2] + \frac{\alpha_2}{\sqrt{2\pi\sigma_2^2}} \times \exp[-(E-E_{C2})^2/2\sigma_2^2] + \frac{\alpha_3}{E_M} \exp(-E/E_M), \quad (1)$$

where the parameters used are listed in Fig. 3 along with a plot of the simulated distribution. The initial positions of all trajectories are distributed evenly along the grid over eight grid spaces. This was necessary since the focusing action of

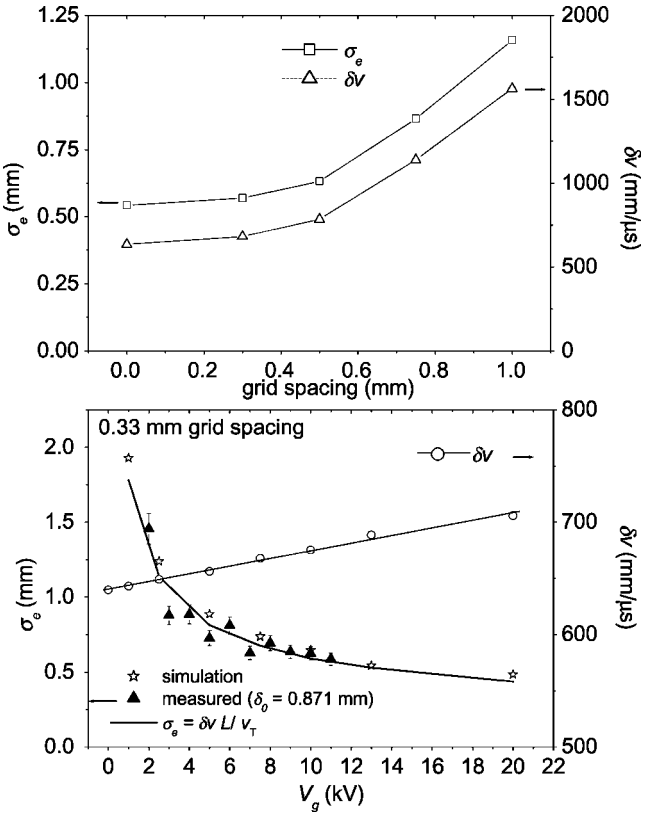

FIG. 4. (a) Broadening of the secondaries as they are transported to the MCP for detection as calculated by Simion 7. A 13 kV potential was used on grids of different mesh size. The rms of the transverse velocity $\delta\nu$ component increases with mesh size, which causes σ_e to increase almost proportionately. (b) Results of simulation showing the σ_e (left axis) and $\delta\nu$ (right axis) dependence on grid potential for a 0.33 mm grid. The solid line is evaluated from an equation that explains what the physical significance of the process is where $\delta\nu$ is taken to be a linear function of the grid potential.

the grid depends on this initial position. The relative displacements were recorded for each trajectory to evaluate the rms displacement σ_e. The results obtained when sampling σ_e, along with the rms transverse velocity $\delta\nu$, are shown in the double axis plot of Fig. 4(a). The grid potential was kept constant at $V_g = 13\,\mathrm{kV}$.

We consider the case where the perpendicular component of the velocity $\nu_\perp$ is nonrelativistic and the transverse component is small compared to $\nu_\perp$. Also, we assume that the acceleration takes place in a region that is negligibly short compared to the drift that follows. Under such conditions we can apply the relation

$$\sigma_e \approx L \cdot \frac{\delta\nu}{\nu_\perp} \approx \delta\nu \sqrt{\frac{L^2 m_e}{2 \cdot V_g e}}, \tag{2}$$

where L is the distance between the dynode and MCP surface, m_e/e is the mass to charge ratio of the electron, and V_g is the acceleration potential. The term in the square root of Eq. (2) is approximately constant; hence σ_e scales very linearly with $\delta\nu$. The transverse velocities are amplified by the grid potentials as the grid spacing becomes larger—especially beyond 0.5 mm. A 0.33 mm spaced copper grid with ~90% transmission was used for this apparatus.

We then turn our attention the broadening dependence on the grid accelerating potential. For a 0.33 mm grid spacing, V_g is varied over some range, and the broadening is better understood if we rewrite Eq. (2) as

$$\sigma_e \approx a \cdot \delta\nu / \sqrt{V_g} = a \cdot \xi(V_g), \tag{3}$$

where a is a constant obtained by comparing with Eq. (2) and the dependence on V_g is absorbed into the function $\xi(V_g)$. A comparison is made between this equation and the results of the Simion simulation in the graph shown in Fig. 4(b). The σ_e (left axis) and $\delta\nu$ (right axis) values are plotted for grid potentials between 0 and 20 kV. The rms transverse velocity seems to increase linearly with accelerating potential, however, only by ~10% throughout this range. The solid line is obtained by Eq. (3) under similar conditions.

Since the rms velocity remains approximately constant, it is possible to decrease the divergence by increasing the grid potential. Going from 5 to 13 kV decreases σ_e by almost 40%. The rate at which σ_e decreases lessens appreciably for higher potentials and will eventually shift to an increase with V_g as $\delta\nu$ will ultimately dominate. The actual limit obtained with our detector seems to be at about 15 kV, at which point the thermionic emission produces considerable noise to the detector.

The dependence on V_g was measured experimentally with a beam spot centered on the dynode surface. The weighed rms moments along the horizontal axis H_{rms} were measured for grid potentials varying from 2 to 11 kV. A constant factor δh_0 is summed in quadrature to σ_e to account for both the finite beam size and broadening due to the electron and photon optics at the MCP. This results all expressed as follows:

$$H_{\mathrm{rms}}^2 = \sigma_e^2 + \delta h_0^2. \tag{4}$$

Fitting this equation with the measured H_{rms} values yields $\delta h_0 = 0.87$ mm if σ_e is evaluated by Eq. (2) and $\delta\nu$ values are taken from a linear fit to the simulation. We solve for σ_e and plot the values in Fig. 4(b). The effect of the grid potential on the broadening seems to be well understood from this result.

IV. MEASURING TRANSVERSE DENSITY DISTRIBUTIONS

The tests with $^{84}Kr^{1+}$ ions from the Dynamitron accelerator have shown that a beam 3.6 or 18 keV/u can be well resolved with an intensity as low as 4×10^2 pps. The latter value is the lowest beam intensity achievable using the attenuators. The maximum intensity could be higher than 200 nA; however, the extent of the grid and MCP detector lifetime may suffer. We did not observe deleterious beam effects even when running up to 10^{12} pps at 1.5 MeV for several hours. A plot of the beam distribution is shown in Fig. 5. Bitmap images of single snap shots of two different beams are illustrated in Fig. 6. Figure 6(a) is that of 18 keV/u krypton ions at rate of 4×10^2 pps. Each resolvable spot represents at least one ion collision event. We point out that the voltage across the MCP system need only be high enough to

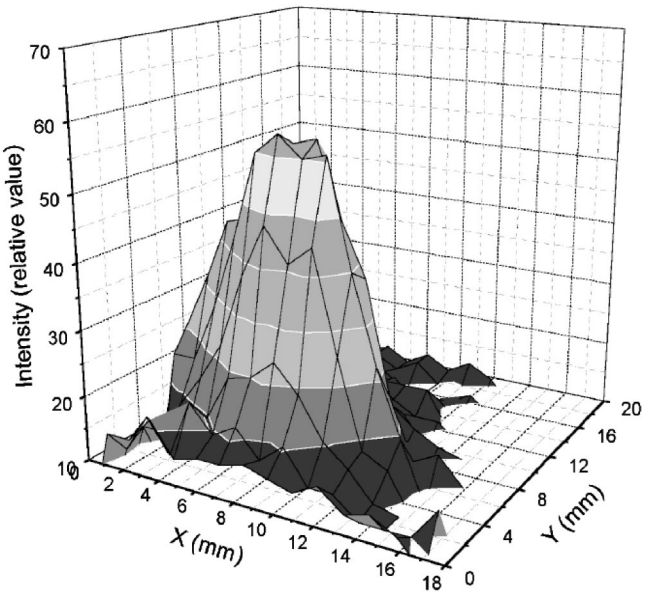

FIG. 5. Transverse beam density distribution obtained for Krypton (2×10^7 pps) beam.

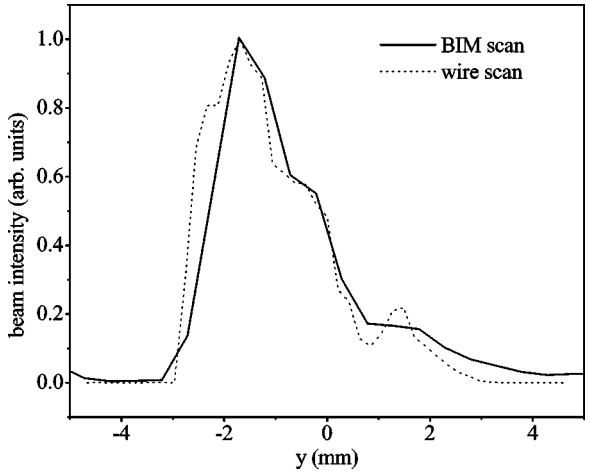

FIG. 7. Beam profiles in the *y* direction measured by both the wire scanner and BIM systems when the grid accelerating potential is 13 kV.

obtain a detectable light intensity when keeping the phospor system at peak sensitivity. This is necessary to extend the lifetime of the MCP.

Since the MCP plates are highly insensitive to gamma radiation, this detection system is sufficiently immune to radioactive decay of a wide range of implanted particles. From a recent experiment we obtained the results illustrated in Fig. 6(b), where a momentum selected, mixed beam of $^{17}F^{9+}$ (67 MeV), $^{16}O^{8+}$ (56 MeV), and $^{16}O^{7+}$ (43 MeV) is striking the conversion surface. The $^{17}F^{9+}$ component constituted 68% of the 2.5×10^5 pps resulting from an inverse kinematics in-flight production technique used at the ATLAS to produce a variety of radioactive species at energies at or below the Coulomb barrier.[12]

At the high intensity limit, the vertical profile of 1 MeV Kr^{1+} beam with an intensity of ~200 nA was measured with both the BIM/slit combination and a 0.25 mm scanned wire. The resulting beam profiles are shown in Fig. 7. The two scans coincide well, which demonstrates that the BIM system is useful for scanning profiles. More experiments will be conducted with the BIM to study its performance under other conditions that may arise.

V. EMITTANCE PROFILE MEASUREMENTS

The previous section demonstrated that profiles in the transverse plane could be measured over a wide dynamic range. This section looks at the performance of such a device when used to measure the transverse phase space character of a beam. Measurements of this type are useful in evaluating the performance of beam transport devices. Typically, one looks for features such as the phase space area and ellipse orientation in terms of the Twiss parameters.[13] With enough spatial and angular resolution, such devices can even offer details about higher order aberration effects.

A schematic diagram of the dual slit plate used for these measurements is shown in Fig. 8. Each slit is 0.2 mm wide and about 45 mm in length. The beam is aligned and focused within a region bounded by a circle of ~30 mm diameter such that each of the two slits scans both the *x* and *y* profiles along separated intervals. The plate is located a distance $L=30.5$ cm upstream from the center of the dynode surface

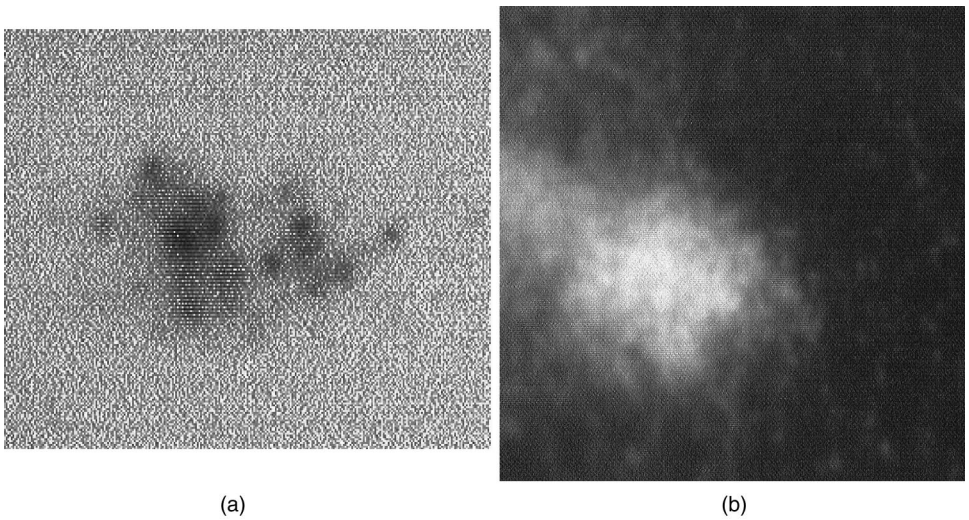

FIG. 6. Beam images of: (a) low intensity $\sim4\times10^2$ pps 18 keV/u krypton beam, area size is 5.1 mm×6.5 mm; (b) total intensity of 2.5×10^3 pps of a radioactive beam line. Area covered in coordinate system of the beam is ~17.0 mm×18.2 mm.

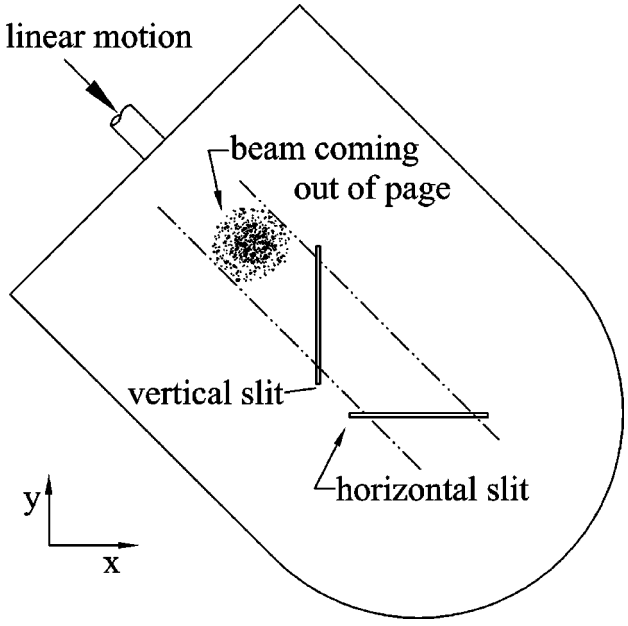

FIG. 8. Double slit plate used to scan both the x and y profiles. The orientation is such that the beam is coming out of the page and the relative beam coordinate axes are labeled on the bottom left.

and a linear feed through that is driven by a step motor is used to scan the plate across the beam in the transverse plane.

At any position of the slit plate, a snap shot can be acquired of the image and recorded at the CID sensor array. An average from multiple snap shots may be processed in order to reduce white noise in cases where the noise to signal level is high. The image is then stored in memory as a two-dimensional (2D) array of 8-bit integers whose intensity is denoted as M_{ij}. The subscripts i and j denote horizontal and vertical position, respectively, of each pixel along the plane of the sensor array. Each snap shot yields a distribution of the beam divergence along the length of the slit. For example, when the beam is in the vertical slit position (see Fig. 8), the intensity will be proportional to the distribution of divergence values x' along the slit that runs along the y axis of the beam coordinate system. Any constants of proportionality derive from a transformation that converts the position values at the sensor array to those of the beam coordinate system (compare Figs. 2 and 8).

The emittance distribution in the $x-x'$ plane is obtained from a series of profiles $M_{ij}(x)$ measured for all x values with the vertical slit. Similarly, the $y-y'$ distribution is obtained from a series of profiles $M_{ij}(y)$ in which the horizontal slit is in the region of the beam. Notice from Fig. 8 that if the linear feed moves in the direction shown by Δr, then there is a corresponding movement of $\Delta x=\Delta r/\upsilon 2$ by the vertical slit and $\Delta y=-\Delta r/\upsilon 2$ by the horizontal. Depending on which slit is in the beam region, a statistical average of the profile is taken by summing values along the orientation of the slit. For example, for every $M_{ij}(x)$ profile we take the sum over the index j

$$H_i(x)=\sum_j M_{ij}(x) \tag{5}$$

to obtain the 1D array with values that represent the average beam intensity along the horizontal direction at the aluminum surface, which is tilted 45° relative to the beam coordinate system. Similarly, a profile along the vertical axis is obtained by

$$G_j(y)=\sum_i M_{ij}(y). \tag{6}$$

Of interest is the rate at which the beam disperses out as drifts from the slit to the aluminum plate, or the divergence of the beam.

To determine the divergence at a given position of the slit we must transform the units of position as referenced at the CID sensor to those of the beam coordinate system. The displacements must be evaluated relative to the slit position by applying the following transformations:

$$h_i=i\cdot k_x-x\cdot\sqrt{2} \quad \text{(vertical slit)}, \tag{7}$$

and

$$g_j=j\cdot k_y-y \quad \text{(horizontal slit)}. \tag{8}$$

Here, h_i represents the corresponding horizontal position at the aluminum plate at pixel row i, and g_j represents the vertical. The constants k_x and k_y are the scale factors that account for the magnification of the tapered fiber optic rod and the distance between each pixel in the horizontal and vertical directions, respectively. Both are taken to be 40.5 ± 0.3 μm/pixel in this setup. The $\upsilon 2$ factor in Eq. (7) accounts for the 45° tilt of the aluminum plate along the horizontal plane

From these arrays we can then evaluate the first and second statistical moments at each position. In the horizontal plane, the second moment h_{rms} is evaluated about the first moment h_m at each x position by taking the square root of

$$h_{\mathrm{rms}}^2(x)=\frac{1}{H_0}\sum_i H_i(h_i-h_m)^2, \tag{9}$$

where H_0 is the integrated profile intensity. Similarly, g_{rms} values are evaluated for each y position. Furthermore, we assume that broadening due to the transport of electrons and photons through the detection system h_d can be accounted for by a deconvolution of Gaussian functions. The convolution theorem dictates that the final rms values of convoluted normal distributions yields another normal distribution with rms value equal to the quadrature sum of each rms component.[14]

Suppose we are interested in rms broadening h_b caused solely by the divergence of the ion beam, then broadening contributed by any other factors σ_d must first be determined before a deconvolution may be applied in obtaining the true broadening caused from the divergence. The dominant component of σ_d here is the broadening of secondaries σ_e; however, there is some contribution σ_{OP} gained due to the limited resolution of the MCP and photon optics. For now, we make the assumption that σ_{OP} is negligible.

As long as it is valid to model the measured rms value of the data as a convolution of distributions with rms values of σ_e and h_b, then we must have

$$h_{\mathrm{rms}}^2 = h_b^2 + \sigma_e^2. \tag{10}$$

The corrected profile H_i^c can be extracted by applying the product of the function $A_i(x)$ with H_i to deconvolute two Gaussian distributions at each x position. This function is obtained from

$$A_i(x) = \exp[-(h_i - h_m)/2h_0^2], \tag{11}$$

where

$$h_0^2 = h_{\mathrm{rms}}^2[(h_{\mathrm{rms}}/\sigma_e)^2 - 1]. \tag{12}$$

The results along the y axis are obtained in the same way. The resulting profiles H_i^c and G_i^c should represent the distribution of ion current density in the coordinate system of the conversion surface. The y' axis coincides with the vertical axis directly but the x' axis does not because of the 45° tilt; therefore, the transformations for finding divergence along each respective axis must be given by

$$y_j' \approx g_j/d_0$$

and

$$x_i' \approx h_i/\sqrt{2}d_0 \tag{13}$$

expressed in units of radians, where d_0 is the distance from the slit to the midpoint of the conversion surface. The deconvoluted emittance profiles obtained by these transformations is shown in Figs. 9(a) and 9(b) for the y and x profiles, respectively. A standard statistical analysis is implemented to extract the rms emittance ϵ_x^* and the Twiss parameters α_x, β_x, and γ_x.[15] The y profile emittance seems to be overpredicted largely due to an aberration that appears at the $+y$ side of the profile. The aberration seemed to be caused by a misalignment between the beam axis and the quadrupole doublet.

The beam current was high enough to scan an emittance profile with the wire scanner, which has a well-defined resolution. From a comparison it seems that the magnitude of the emittance measured by the BIM is about twice as large as the wire scanner measurements. This is largely due to the fact that the divergence is very small for the $L = 30.5$ cm drift between the slit and spatial dispersion. Aside from a possible future test, enough information on the BIM system has been obtained to assess its usefulness as an emittance profile device. It is estimated that the rms spatial width from the divergence is no greater than 0.12 mm, which makes it difficult to extract the profile by deconvolution. The present setup at the Dynamitron allows only relatively small emittances to be transported to the slit without loss of beam, thus the only future solution will be to increase L threefold to obtain enough spatial dispersion. Aside from a possible future test, enough information on the BIM system has been obtained to assess its usefulness as an emittance profile device.

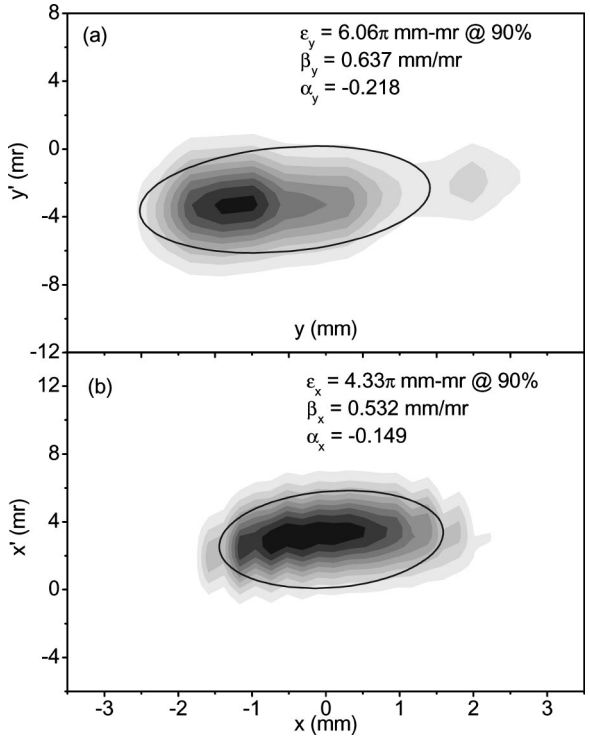

FIG. 9. Emittance profiles extracted from the divergence profiles. The ellipse drawn fits the phase space area given by ϵ_x and ϵ_y. If the distributions were truly Gaussian in form then 90% of the total beam intensity would lie within this boundary. The Twiss parameters and rms emittance were evaluated by a statistical analysis.

ACKNOWLEDGMENTS

This work supported by the U. S. Department of Energy, Nuclear Physics Division, under Contract W-31-109-ENG-38. Special thanks go to S. Sharamentov for his technical assistance in constructing the electrical hardware, and also to R. Pardo and J. Nolen for their valuable remarks and discussions.

[1] Simion 7, Scientific Instrument Services, 1027 Old York Rd., Ringoes, NJ 08551.
[2] J. L. Forand *et al.*, Rev. Sci. Instrum. **61**, 3372 (1990).
[3] Colutron Research Corporation. http://www.colutron.com/
[4] D. Shapira, T. A. Lewis, L. D. Hulett, Jr., and Z. Ciao, Nucl. Instrum. Methods Phys. Res. A **449**, 396 (2000).
[5] K. Kruglov *et al.*, Nucl. Instrum. Methods Phys. Res. A **441**, 595 (2000).
[6] A. V. Feschenko *et al.*, Proceedings of the 1996 Linac Conference, Chicago, IL, 1996, p. 193.
[7] H. Rothard *et al.*, Nucl. Instrum. Methods Phys. Res. B **48**, 616 (1990).
[8] E. Bauer, Vacuum **22**, 539 (1972).
[9] A. Albert, K. Kroneberger, O. Heil, and K. O. Groeneveld, Nucl. Instrum. Methods Phys. Res. A **317**, 397 (1992).
[10] L. A. Dietz and J. C. Sheffield, Rev. Sci. Instrum. **44**, 183 (1973).
[11] L. A. Dietz and J. C. Sheffield, J. Appl. Phys. **46**, 4361 (1975).
[12] R. Pardo, B. Harss, K. E. Rehm, J. Greene, D. Henderson, C. L. Jiang, J. P. Shiffer, J. R. Specht, and B. J. Zabransky, *15th International Conference on the Application of Accelerators in Research and Industry*, Denton, TX 1998, edited by J. L. Duggan and I. L. Morgan (American Institute of Physics, Woodbury, NY, 1998).
[13] H. Wollnik, *Optics of Charged Particles* (Academic, Orlando, FL, 1987), Chap. 5, p. 154.
[14] E. Parzen, *Modern Probability Theory and Its Applications* (Wiley, New York, 1960), p. 317.
[15] M. Reiser, *Theory and Design of Charged Particle Beams* (Wiley, New York, 1994), p. 56.